Title

Digital holographic inspection system for the inner surface of a straight pipe

Author(s)

Masayuki Yokota, Teppei Koyama, and Kazufumi Takeda

Journal

Optics and Lasers in Engineering

Volume 97, October 2017, Pages 62-70

Published

2017

URL

https://doi.org/10.1016/j.optlaseng.2017.05.012

Digital holographic inspection system for the inner surface of a straight pipe

Masayuki Yokota, Teppei Koyama, and Kazufumi Takeda

Interdisciplinary Faculty of Science and Engineering, Shimane University

1060 Nishikawatsu-cho, Matsue, Shimane 690-8504, Japan

Tel: +81-852-32-6349, Fax: +81-852-32-8909

E-mail: yokota@ecs.shimane-u.ac.jp

Abstract

A multicolor digital holographic inspection system achieving both automatic scanning sensing head and automatic correction of a distortion in the profile due to positional error of a sensing head has been applied to the inner surface of a straight brass pipe having artificial defects on its wall. To investigate the inner surface of the pipe, the sensing head consisting of a cone-shaped mirror (CSM) glued to an aluminum base in the pipe is illuminated by the collimated RGB laser beams from the outside of the pipe. In the system, by changing the wavelength of the illumination light and scanning the CSM in the pipe, data acquisitions and analysis are performed using a personal computer. It is shown that the pipe inspection, including a classification of defects, can be successfully conducted by comparing the multicolor intensity images and the height profile of inner surface of pipe.

Key words: digital holographic system, holographic interferometry, multiwavelength, pipe inspection

1. Introduction

Maintenance of pipes used in our living environment is necessary for their stable operations. For ensuring the safety of pipe systems, measurement of the inner surfaces of pipes should be conducted periodically to assess their conditions. In addition, the investigation of inner cylindrical surfaces such as engine cylinders or barrels is also an important demand for many fields in industry. For this purpose, many optical methods have been proposed to measure the inner surface of pipes including both

straight and curved ones [1-4]. In the single spot scanning method, the location of a light spot projected on the pipe inner wall is detected using a position sensing device, and three- dimensional coordinates of the inner wall can be constructed by helically rotating the light spot [1]. Optical sectioning methods using a specific pattern such as helical fringes [2] or a single ring [3] have been proposed for pipe inspection. In the above methods, the wireframe image of the pipe inner surface can be obtained and used to detect both the inner diameter and surface defects. An optical stylus method using white-light interferometry has been applied to the inspection of engine cylinder walls [4]. A vertical resolution of 1 nm rms has been achieved with the optical stylus measurement system. However, both the visualization and profilometry of the inner wall of pipes or cylinders have not been realized in the proposed optical methods.

To achieve the imaging and profile measurement of the pipe inner wall, we have introduced digital holography for straight pipe inspection [5-7]. In digital holography [8,9], the external appearance of objects can be confirmed in the focused reconstructed intensity image of digital holograms. For surface shape measurements, digital holographic interferometry can be used, in which two-wavelength method using the injection-current induced wavelength change of laser diode has been adopted in our system.

To inspect the pipe inner wall, a cone-shaped mirror (CSM) is inserted into the pipe and then illuminated by a collimated laser beam. In the first manuscript [5], it was suggested that the distorted surface profile due to the deviation of CSM from the pipe axis could be corrected by subtracting an asymmetrical distribution of optical path length around the CSM in the pipe. Next, the efficacy of the proposed correction process using the asymmetrical optical path length distribution has been experimentally verified by adding a known deviation to the CSM mirror in the pipe [6]. Recently, the multiwavelength digital holographic method using two red laser diodes has been proposed for the pipe inspection [7]. In the method, both the imaging and profile measurement of artificial defects on the inner wall of a copper pipe has been demonstrated by connecting 31 reconstructed images at the different positions of the CSM in the pipe. To scan all the defects in the pipe, the CSM in the pipe was shifted manually using a mechanical stage. The classification of defects using the difference in

the spectral reflectance obtained for the reconstructed intensity images was not succeeded due to small wavelength difference in two red laser diodes. To correct the distortion of the height profile, the calculation of an optical path length between the CSM surface and the corresponding pipe wall is required. However, the correction process requires the coordinates of the center point of the CSM in reconstructed images, which we have estimated visually so far [7].

In this paper, we describe the novel automatic measurement system for a straight pipe inner surface using both multiwavelength color phase-shifting digital holography and holographic interferometry. Further, the pattern matching technique to estimate the center point of the reconstructed CSM image has been newly introduced into the correction process for the inner surface profile. By virtue of the pattern matching technique, the signal processing for obtaining a corrected surface profile can be automatically performed using a personal computer (PC). In addition, data acquisition in which phase shifting holograms of the inner wall are recorded for four wavelength has been conducted automatically by shifting the CSM position with a PC-controlled stepping motor. The system has been applied to the inspection of a straight brass pipe (14.0 mm inner diameter) having artificial defects on its inner wall. By using both differences in the spectral reflectance of RGB-intensity images and a surface profile image of the inner wall, discrimination of defects has been successfully demonstrated.

2. Signal processing

2.1 **Surface contouring by digital holographic interferometry**

In phase-shifting digital holography [10], the light wave reflected from an object surface is interfered with the phase-shifted reference light wave at an imaging device such as a charge coupled device (CCD) camera. When the interference pattern of the hologram is digitized by the CCD having $N \times N$ pixels and pixel pitches of $\Delta x \times \Delta y$ along the coordinates, the complex amplitude of the object wave $U(m\Delta x, n\Delta y)$ is calculated by using four phase-shifting holograms as

$$U(m\Delta x, n\Delta y) = \frac{1}{4U_r^*(m\Delta x, n\Delta y)}\{I(m\Delta x, n\Delta y; 0) - I(m\Delta x, n\Delta y; \pi) + i[I(m\Delta x, n\Delta y; \tfrac{\pi}{2}) - I(m\Delta x, n\Delta y; \tfrac{3\pi}{2})]\}, \quad (1)$$

where m and n are integers varying from -N/2 to N/2-1, $U_r^*(m\Delta x, n\Delta y)$ is the complex conjugate of the amplitude of reference wave, $I(m\Delta x, n\Delta y;\delta)$ denotes the hologram intensity at the CCD plane, and $\delta = 0$, $\pi/2$, π, and $3\pi/2$ is the magnitude of the phase shift for the reference wave.

For the reconstruction of the object wave, the complex amplitude $U_I(l\Delta X, p\Delta Y; Z)$ at a distance Z from the CCD surface can be obtained by calculating the numerical Fresnel transformation of

$$U_I(l\Delta X, p\Delta Y; Z) = exp\left[i\frac{\pi}{\lambda Z}(l^2\Delta X^2 + p^2\Delta Y^2)\right] DFT\left\{U(m\Delta x, n\Delta y; 0) exp\left[i\frac{\pi}{\lambda Z}(m\Delta x^2 + n\Delta y^2)\right]\right\}, \quad (2)$$

where l and p are integers varying from -N/2 to N/2-1, and $DFT\{\}$ means discrete Fourier transformation. In hologram reconstruction using Eq. (2), the pixel pitches of both ΔX and ΔY at the reconstructed image plane along X and Y axis, respectively, become

$$\Delta X = \frac{\lambda Z}{N\Delta x}, \ \Delta Y = \frac{\lambda Z}{N\Delta y}. \quad (3)$$

Therefore, the magnitude of the pixel pitches at the reconstructed image plane depends on both the wavelength λ and the distance Z [11]. For further analysis of the images reconstructed at different λ or Z, the size of the pixel pitches of the images should be equalized among all the reconstructed images. To achieve equalization of the pixel pitches, the zero-padding method has been used [12]. To equalize the pixel pitches between the reconstructed images for both λ_1 and λ_2, where $\lambda_2 > \lambda_1$, the pixel number N_2 of the image for λ_2 should be adjusted to

$$N_2 = N_1\frac{\lambda_2}{\lambda_1}. \quad (4)$$

The number of pixels can be easily modified by padding zeros to the original image matrix.

For surface contouring of a pipe inner wall using the two-wavelength method [13-20], four phase-shifting holograms are recorded for two wavelengths of λ_1 and λ_2. When the laser beam normally illuminates the inner wall of the pipe, the phase difference $\Delta\phi$ between the phases of the object waves reconstructed individually for λ_1 and λ_2 expresses a height profile of the wall as

$$\Delta\phi(l\Delta X, p\Delta Y) = arg\langle U_{I1}(l\Delta X, p\Delta Y)U_{I2}^{*}(l\Delta X, p\Delta Y)\rangle = \frac{4\pi h(l\Delta X, p\Delta Y)}{\Lambda}, \quad (5)$$

where $U_{I1}(l\Delta X,p\Delta Y)$ and $U_{I2}(l\Delta X,p\Delta Y)$ are the reconstructed complex amplitudes for the wavelength λ_1 and λ_2, respectively, $h(l\Delta X,p\Delta Y)$ is the surface height of object, $\Lambda = \frac{\lambda_1\lambda_2}{|\lambda_1-\lambda_2|}$ is the synthetic wavelength, $\langle\ \ \rangle$ is the averaging, and the phase difference is obtained as the phase of the averaged conjugate product for a speckle noise reduction [21]. The height range corresponding to $\Delta\phi = 2\pi$ is given by $\Delta h = \Lambda/2 = \lambda_1\lambda_2/2|\lambda_1-\lambda_2|$.

2.2 Correction process for a height profile

To obtain a precise profile of the inner wall of straight pipes, the center of CSM must be scanned along the pipe axis. When the center of CSM coincides with the pipe axis, the distance between the mirror edge and the pipe inner wall becomes constant. However, in the actual scanning process, the center of the CSM deviates from the pipe axis, which generates an asymmetrical optical path length distribution between the mirror surface and the inner wall of the pipe. The resultant asymmetrical optical path length distribution is added to the value $\Delta\phi$ in Eq. (5) as unwanted bias. To correct the distorted inner surface profile obtained from the biased $\Delta\phi$, the optical path length distribution between the mirror surface and the inner wall is required.

For the purpose, a simple model in Fig. 1 representing the arrangement of the CSM in the straight pipe in which the center O' of the CSM deviates from the pipe axis O by d is considered. In the configuration, the optical path length $L(m,n)$ between a point P(m,n) on the observation plane S and

the corresponding point R on the pipe inner wall is considered. When the inclination of the CSM towards the pipe axis is neglected, the optical path length $L(m,n)$ is equal to $\overline{PQ} + \overline{QR}$.

Considering the case where the observation plane S is set on the top of the CSM in Fig. 1(b), the optical path length $L(m,n)$ equals to $r + L_e(\theta)$, where r is the radius of the CSM and $L_e(\theta)$ is the distance UT between the edges of the CSM and the pipe inner wall along the orientation θ. For calculating $L_e(\theta)$, a theorem of cosines is applied to the triangle OO'U in Fig. 1(a).

$$OU^2 = OO'^2 + O'U^2 - 2OO' \cdot O'Ucos(\angle OO'T) = d^2 + [r + L_e(\theta)]^2 - 2d[r + L_e(\theta)]cos(\pi - \theta) \quad (6)$$

where $OU = R_p$ is the radius of the pipe, d is the center-to-center distance between O(0, 0) and O'(ε_x, ε_y) obtained as $(\varepsilon_x^2+\varepsilon_y^2)^{1/2}$. Solving Eq. (6) for $r+L_e(\theta)$, the optical path length $L(m,n)$ between the points $P(m,n)$ and $R(m,n)$ can be obtained as

$$L(m,n) = r + L_e(\theta) = -dcos\theta + \sqrt{R_p^2 - d^2 sin^2\theta} \ . \quad (7)$$

As seen in both Fig. 1(a) and Eq. (7), the magnitude of $L(m,n)$ depends directly on the value of $L_e(\theta)$. Therefore, the value of $L_e(\theta)$ can be evaluated from the distorted experimental profile including the variation of $L_e(\theta)$. Both the values of ε_x and ε_y can be obtained from the next relationship

$$\begin{cases} d = (L_{emax} - L_{emin})/2 \\ \varepsilon_x = dcos(\theta_m) \\ \varepsilon_y = dsin(\theta_m) \end{cases}, \quad (8)$$

where $L_{emax(emin)}$ is the maximum or minimum value of L_e, and θ_m is the orientation angle giving the value of L_{emin}. For calculating the path length distribution $L(m,n)$, both the values of d and θ_m must be estimated by fitting the curve of Eq. (7) to the experimental height variation along the circumference of circular CSM image [7]. To complete the process automatically, the center of the CSM image is obtained by the newly proposed pattern matching method described in Section 4.

3. Experimental configuration

3.1 Optical setup of digital holographic system

Fig. 2(a) shows the experimental setup for inspecting an inner wall of a straight pipe. To obtain both a multiwavelength intensity image and a surface profile of the pipe inner wall, two diode-pumped solid state (DPSS) lasers having different wavelengths and a laser diode (LD) are used as the light sources in the system. The DPSS lasers have wavelengths of λ_3 = 532.5 nm for DPSS1 (CNI, MSL-3-532) and λ_4 = 473.2 nm for DPSS2 (CNI, MSL-FN-473). The injection current of LD (Hitachi, HL6362MG) is changed by a modulation signal producing a wavelength of either λ_1 = 639.1 nm or λ_2 = 639.2 nm. Thus, using a pair of λ_1 and λ_2, the synthetic wavelength of $\Lambda_{12} = \lambda_1\lambda_2/|\lambda_1-\lambda_2| = 4.09$ mm can be obtained for digital holographic contouring of the pipe inner wall. When the other wavelength pairs including either λ_3 or λ_4 are used for a surface contouring, the synthetic wavelength Λ becomes less than 10 μm due to the large wavelength difference of more than 60 nm. Therefore, for the surface contouring of the pipe inner wall having artificial defects, only the pair of λ_1 and λ_2 has been adopted for analysis.

The output beams from the three lasers are combined using two single-mode fiber couplers. The output beam from the end of the fiber coupler is collimated and then divided by a polarization beam splitter (PBS) into two optical paths. The beam reflected from a piezoelectric transducer (PZT: P.I., P-753.12C) mirror acts as a reference beam. The other beam incident on the CSM in the straight pipe illuminates the inner wall of the pipe. The beam reflected from the inner wall becomes an object beam. Quarter-wave plates ($Q_{2,3}$) and polarizers ($P_{2,3}$) are used to reduce the reflected beams from the surface of the optical components. In measurements, a straight brass pipe of 100 mm length and 14.0 mm inner diameter was used. As shown in Fig. 2(b), the CSM glued to the end surface of an aluminum base with 13.6 mm diameter and 37.0 mm length becomes a sensing head. For the measurement, the sensing head was inserted into the pipe and scanned along the pipe axis. The end of the aluminum base was connected with a line 0.26 mm in diameter, which was wound using a bobbin rotated by a

PC-controlled stepping motor. Thus, the location of the sensing head in the pipe was decided by controlling the rotation of the stepping motor.

The wavelength of the light illuminating the pipe inner wall was selected by using a PC-controlled modulation signal. Both the injection current for the LD and the operation of the electromagnetic shutter for the DPSS lasers are controlled by supplying a voltage signal from a D/A board (Interface, PCI-3336) in the PC. The wavelength of the LD is monitored using an optical spectrum analyzer (Advantest, Q8344A). Four phase-shifting holograms formed with each laser beam are captured sequentially by a CCD camera (Hamamatsu photonics, C4742-95-12ER) having 1024×1024 pixels with a pixel size of 6.45×6.45 μm and 12-bit grayscale, and then stored in a frame grabber of the PC. After the hologram recordings, the sensing probe was moved to the next position by rotating the PC-controlled stepping motor. The process of data acquisition was automatically repeated for inspecting the pipe inner wall.

Fig. 3 shows a flow chart of hologram recording processes for the pipe inspection. At first, the wavelength of LD is set to λ_1 = 639.1 nm by applying the voltage V_1 = 1.188 V to a laser driver for LD and four phase-shifting holograms are captured by the CCD. Then, another set of phase-shifting holograms are recorded by changing the wavelength of LD to λ_2 = 639.2 nm with the application of voltage V_2 = 1.089 V for the laser driver. After turning off the LD, the electromagnetic shutter S1 for DPSS1 is opened by supplying the signal VS_1 to the shutter and then phase-shifting holograms are recorded for λ_3 = 532.5 nm. Finally, after closing the shutter S1, the shutter S2 for DPSS2 is opened by the signal VS_2 and phase-shifting holograms for λ_4 = 473.2 nm are recorded. After completing the above hologram recording process, the CSM rod is pulled by 1.0 mm using the stepping motor. All the processes were automatically performed by the PC and repeated N = 63 times to detect all the artificial defects on the inner wall of a pipe.

3.2 Configuration of the straight brass pipe for test

Fig. 4 shows the configuration of the brass pipe having the artificial defects on its inner wall and the pictures of them. At first, the top of the CSM rod inserted in the pipe was set at a position of Δz = 0.0

mm in Fig. 4(a). The recording distance of the hologram between the CCD plane and the CSM rod for Δz = 0.0 mm corresponded to z_0 = 280 mm. The measurement was conducted by moving the CSM rod along the direction of the arrow with a constant step of 1.0 mm. The artificial defects of 1, scratch_1; 2, scratch_2; 3, an aluminum sheet having a size of 3.36×11.92×0.36 mm; 4, a copper sheet having a size of 2.68×8.34×0.27 mm; and 5, verdigris, were pasted or made on the inner wall, as shown in Fig. 4(a). The pictures of the defects are shown in Fig. 4(b). To detect all the defects, the CSM was moved 1.0×63 = 63.0 mm along the direction of the arrow by rotating the stepping motor driving bobbin. In that case, the defect could be detected in numerical order.

4. Experimental results

4.1 New automatic correction method using the pattern matching algorithm for detecting the image center

As post signal processing to remove the asymmetric optical path length distribution due to misalignment of the CSM from the experimental height profile, a novel automatic correction method using pattern matching algorithm for detecting the center of the CSM image has been introduced. For calculating the optical path length distribution, the center of the CSM image has to be detected, which was conducted manually in the past method [6,7].

To detect the center of the CSM image, a template circle image having the same diameter as that of the CSM image was used for the pattern matching process. As an example, the experimental results obtained for Δz = 35.0 mm are used as shown in Fig. 5(a). The recording distance between the top of the CSM and the CCD plane was $z_0+\Delta z$ = 315.0 mm. In the reconstructed intensity image with Δz = 35.0 mm, no defect was observed. In the system, the pixel pitches in the reconstructed images depend on the wavelength because of Fourier transformation of hologram reconstruction [10,11]. To adjust the size of the pixel pitches for the reconstructed images with different wavelengths and distances Z, the zero-padding method was applied [12], and the size of pixel pitches were adjusted to the pixel size obtained for Δz = 0.0 mm (i.e., z_0 = 280.0 mm) with a wavelength λ_4 = 473.2 nm. In this case,

the pixel pitch was calculated as $\Delta X = \Delta Y = 20.1$ μm.

Fig. 5(b) shows the binarized image of the reconstructed intensity in Fig. 5(a). For binarizing the image, the threshold intensity value for binarization was decided using the p-tile method based on the histogram of the intensity values [22]. By performing pattern matching between the binarized image and the template one, it was possible to detect the position of the center of the CSM image (O_x, O_y) = (496, 554). Fig. 6(a) shows the experimental height profile with a distortion due to the misalignment of the CSM. In Fig. 6(a), the white dotted circle with a radius 70% of the circular image radius was illustrated using the evaluated image center (496, 554). The height variation along the dotted circle is shown in Fig. 6(b) with solid line. The dotted curve in Fig. 6(b) is the least square fitting curve of Eq. (7) to the experimental height variation shown as solid line. By applying the same procedure described in the previous work [7] and Eq. (8), the positional misalignment of both ε_x and ε_y can be evaluated as -0.0387 mm and -0.0101 mm, respectively. Figs. 6(c) and 6(d) show the calculated optical path length distribution $L(X,Y)$ using the positional misalignment of the CSM and the corrected height profile $h_c(X,Y)$, respectively. As seen in Fig. 6(e), the distortion occurring in the surface profile due to the positional misalignment of the CSM can be effectively reduced by the new automatic correcting procedure. Finally, the corrected height profile is transformed to the rectangular image corresponding to the illuminated inner surface by using simple image processing, as shown in Fig. 7 [6,7]. For connecting all the experimental profiles, a part of the rectangular image having a width of 1.0 mm within the dotted rectangular was used for the further process.

4.2. Analysis of artificial defects on the inner wall using both intensity images and height profile

To visualize all the defects, the rectangular intensity images were combined to show the entire measured area of the pipe inner surface. Fig. 8 shows the combined intensity images from $\Delta z = 0.0$ mm to 63.0 mm for three wavelengths $\lambda_1 = 639.1$ nm, $\lambda_3 = 532.5$ nm, and $\lambda_4 = 473.2$ nm. Therefore,

the area of 63.0 mm in length and 44.0 mm in width of the inner wall is displayed in Fig. 8. In Fig. 8(a), the white dotted areas show the artificial defects described in Fig. 4. As can be seen, all the defects can be recognized in all intensity images for different wavelengths. Bright areas are visible in both the left and right sides of the image. The areas might have smooth surfaces to reflect maximum amount of illuminating beams. As seen in the three intensity images, the intensity of 5: verdigris becomes lower than the other area. While the defects can be recognized in all the intensity images, it is difficult to classify them by using an intensity image obtained by a single wavelength.

To investigate the differences in the spectral reflectance of the two metal sheets and verdigris, the intensity ratio $\overline{I_{defect}}/\overline{I_{surface}}$ between the defect and the inner surface without a defect are calculated and shown in Fig. 9. For averaging the intensity I_{surface}, two areas within the dotted lines in Fig. 8(b) were used. In the area of verdigris, all the intensity ratios for the three wavelengths become less than 0.1 and no significant wavelength dependence is observed in the results. This is because the surface of verdigris became rough due to erosion, and scattered the incident light much more than the other surface. In comparison between the Al and the Cu sheets, the intensity ratios of the Al sheet for both blue and green wavelengths become more than twice that of the Cu sheet. The results seem to be reasonable by considering the difference in spectral reflectance for aluminum and copper. By means of the wavelength dependence in spectral reflectance of objects, it is possible to classify the defects on the inner wall of the pipe.

Fig. 10 shows the combined height profile displaying the same areas of intensity images in Fig. 8. While the defect 2: scratch_2 can be observed in all the intensity images in Fig. 8, it is difficult to recognize scratch_2 in the height profile image. The depth of the groove in scratch_2 might be too small to be detected in the height profile. Both the height profile and the relative position of the other defects are adequately reconstructed in Fig. 10. The relatively rough surface is confirmed in the area between X = 1500 and 2000 pixels. The area of the rough surface in Fig. 10 almost corresponds to the dark portion of the intensity images in Fig. 8. Part of the reason for the rough surface might be a low reliability of the phase value at the low amplitude of the object wave. The same roughness and low reliability of the phase can be observed in the area of 5: verdigris. The height profile of verdigris

becomes incorrect, as seen in Fig. 10.

To investigate the height profile of each defect, several cross-sectional height variations are obtained along X or Y direction, as shown in Fig. 11. As seen in both Figs. 11(a) and 11(d), the height profile of the Al sheet can be evaluated from the result, and the surface profile of verdigris becomes less reliable due to the same reason described above. The depth of scratch_1 is well represented and recognized in Fig. 11(c). In Fig. 11(b), the height profile along X = 1400 becomes rough in comparison with that along X = 630 in Fig. 11(a). The area of X = 1400 is included within the dark portion of the intensity images and that probably degrades the height profile. While the profile of the Cu sheet can be detected in both Figs. 11(b) and 11(e), the shape of the Cu sheet is blurred in comparison with that of the Al sheet. The degradation of the profile of the Cu sheet can be attributed to both low reflectivity of the Cu sheet in Fig. 9 and the low intensity distribution of the pipe surface in Fig. 8(a). The length of the metal sheets along the longer direction of the pipe is over estimated by about 10% as compared with the original size shown in Fig. 4(b). This over estimation in size might be due to the positional uncertainty of the CSM sensing head. The accuracy of the movement of the CSM sensing head by the stepping motor system was estimated to be 0.97±0.09 mm, obtained by averaging 28 steps of 1.0-mm-step movement. The accumulation of the positional error resulted in the over estimation of the length of the metal sheets.

The discontinuity in the Y-direction seen in a previous work with a step of 3.0 mm [7] is not clearly seen in the results of both Figs. 8 and 10. Since the lower part of the rectangular images shown in Fig. 7 can avoid the highly distorted area due to the rectangular-to-circular image conversion [6,7], the combined images effectively represent a structure of the surface. In addition, the new correction process can effectively work to reduce the distortion in height profiles.

Fig. 12 shows the evaluated positional error of the CSM obtained with the new pattern matching method. Most of the error exists within ±0.2 mm for both ε_x and ε_y. Some of the detected errors having the number of 4 or 5 in Fig. 12 exceed 0.2 mm. These errors correspond to the areas including the defect of 4: Cu sheet or 5: verdigris. To evaluate the error from the experimental height profile, it is difficult to completely fit the curve of Eq. (7) to the profile curve having a large defect, which results

in misleading the correction process. For further analysis, the correction for such an area becomes a problem. As seen in the results, all the defects can be detected and classified by using both the height profile and the intensity images reconstructed with three wavelength.

5. Conclusions

We have presented a multiwavelength digital holographic inspection system for the inner surfaces of straight pipes. To achieve automatic data acquisition for a pipe inner wall, the position of the cone-shaped mirror sensing head in the pipe is controlled by newly developed stepping motor system. In addition, the new pattern matching method has been introduced into the correction process for inner surface profiles. By virtue of both the developed data acquisition system and analysis, the measurement of a straight pipe inner wall can be automatically performed.

By applying the system to the inspection of a straight brass pipe having several artificial defects on its inner wall, some applications and advantages are shown in the experimental results. To classify the defects, multiwavelength intensity images play an important role to investigate the difference in their spectral reflectivity. For a precise measurement of inner surface, digital holographic interferometry can increase the usefulness of the inspection system.

For further analysis, both fast data acquisition and color estimation are highly important to strengthen the advantages of the system [23,24]. In addition, the correction process considering the inclination of the CSM to the pipe axis will be quite useful to increase the accuracy of profile measurements.

5.1 Acknowledgement

This work was supported by MEXT KAKENHI Grant Number 24560521.

References

1. Wu E, Ke Y, Du B. Noncontact laser inspection based on a PSD for the inner surface of minidiameter pipes. IEEE Transactions on Instrumentation and Measurement 2009; 58(7): 2169-

73.

2. Alvertazai AG, Hofmann AC, Fantin AV, Santos JMC. Photogrammetric endoscope for measurement of inner cylindrical surfaces using fringe projection. Appl Opt 2008; 47(21): 3868-76.
3. Zhang WW, Zhuang BH. Non-contact laser inspection for the inner wall surface of a pipe. Meas. Sci. Technol 1998; 9(9): 1380-87.
4. Windecker R. High resolution optical sensor for the inspection of engine cylinder walls, Optik 2001; 112(9): 407-12.
5. Yokota M, Ishitobi N, Estimation of inner surface profile of a tube by two-wavelength phase-shifting digital holography. Opt Rev 2010; 17(3): 166-70.
6. Yokota M, Adachi T, Digital holographic profilometry of the inner surface of a pipe using a current-induced wavelength change of a laser diode. Appl Opt 2011; 50(21): 3937-46.
7. Yokota M, Kawakami T, Koyama T, Digital holographic inspection for the inner surface of a straight pipe using current-induced multiwavelength from two laser diodes. Opt Eng 2014; 53(10): 104103-1-7.
8. Juptner W, Schnars U. Digital Holography, (Springer Verlag, 2004).
9. Kreis T. Holographic interferometry-optical and digital methods (Wiley-vch GmbH&Co.KGaA; 2005.
10. Yamaguchi I, Zhang T, Phase-shifting digital holography. Opt Lett 1997; 22(16): 1268-70.
11. Schnars U, Juptner W, Direct recording of holograms by a CCD target and numerical reconstruction. Appl Opt 1994; 33(2): 179-81.
12. Javidi B, Ferraro P, Hong S, Nicola SD, Finizio A, Alfieri D, Pierattini G, Three-dimensional image fusion by use of multiwavelength digital holography. Opt Lett 2005; 30(2): 144-6.
13. Yamaguchi I, Ida T, Yokota M, Surface shape measurement by phase-shifting digital holography with a wavelength shift. Appl Opt 2006; 45(29); 7610-6.
14. Wada A, Kato M, Ishii Y, Large step-height measurements using multiple-wavelength holographic interferometry with tunable laser diodes. J Opt Soc Am A 2008; 25(12): 3013-20.

15. Mann CJ, Bingham PR, Paquit VC, Tobin KW, Quantitative phase imaging by three-wavelength digital holography. Opt Express 2008; 16(13): 9753-64.

16. Fu Y, Pedrini G, Hennelly BM, Groves RM, Osten W, Dual-wavelength image-plane digital holography for dynamic measurement. Opt Laser Eng 2009; 47(5)**:** 552-7.

17. Tankam P, Picart P, Use of digital color holography for crack investigation in electronic components. Opt Laser Eng 2011; 49(11)**:** 1335-42.

18. Desse JM, Picart P, Tankam P, Digital color holography applied to fluid and structural mechanics. Opt Laser Eng 2012; 50(1): 18-28.

19. Williams L, Banerjee PP, Nehmetallah G, Praharaj S, Holographic volume displacement calculations via multiwavelength digital holography. Appl Opt 2014; 53(8): 1597-603.

20. Carl D, Fratz M, Pfeifer M, Giel DM, Hofler H, Multiwavelength digital holography with autocalibration of phase shifts and artificial wavelengths. Appl Opt 2009; 48(34): H1-8.

21. Yamaguchi I, Yokota M, Speckle noise suppression in measurement by phase-shifting digital holography. Opt Eng 2009; 48(8)**:** 085602-1-6.

22. Al-amri SS, Kalyankar NV, Khamitkar SD, Image segmentation by using threshold techniques. Journal of Computing 2010; 2(5): 83-6.

23. Nomura T, Imbe M, Single-exposure phase-shifting digital holography using a random-phase reference wave. Opt Lett 2010; 35(13): 2281-83.

24. Ito Y, Shimozato Y, Xia P, Tahara T, Kakue T, Awatsuji Y, Nishio K, Ura S, Kubota T, Matoba O, Four-wavelength color digital holography. J. Display Technol 2012; 8(10): 570-6.

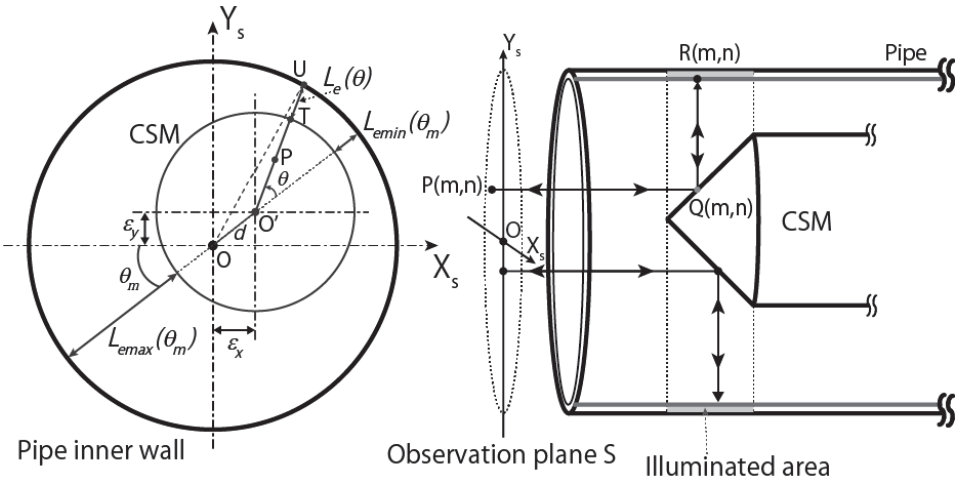

(a) View from the plane S (b) CSM in the pipe

Fig. 1 Arrangement of the CSM deviating (ε_x, ε_y) from the pipe axis in plane S: (a) view from plane S and (b) the CSM head in the pipe and the optical path length L(m,n) = PQ(m,n)+QR (m,n) at the point P(m,n) on plane S.

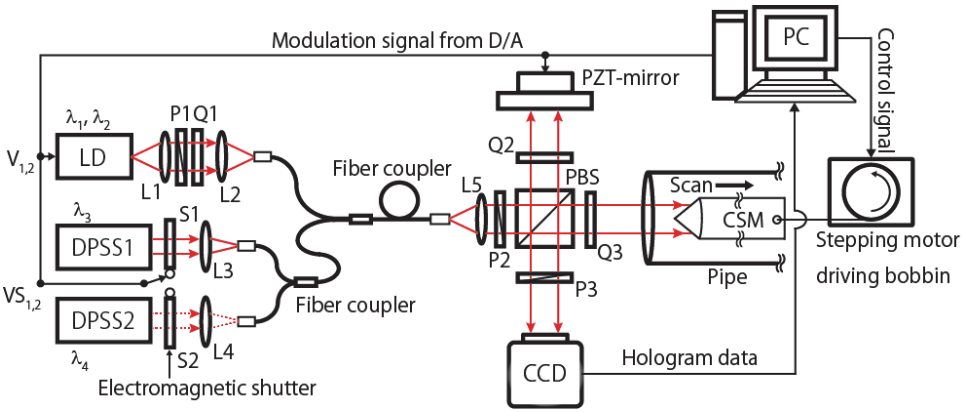

(a) Experimental setup

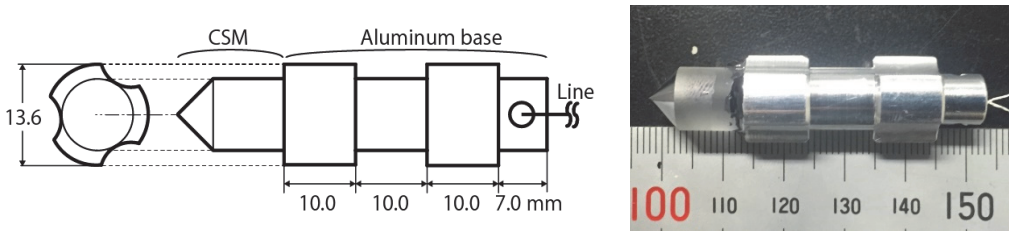

(b) CSM sensing head

Fig. 2 Configuration of the measurement system for a pipe: (a) experimental setup; LD, laser diode; DPSS, diode pumped solid state laser; L, lens; Q, $\lambda/4$ plate; P, polarizer; CCD, charge coupled device; PBS, polarization beam splitter; CSM, cone-shaped mirror; PC, personal computer; PZT, piezo-electric transducer, (b) CSM sensing head used in the system.

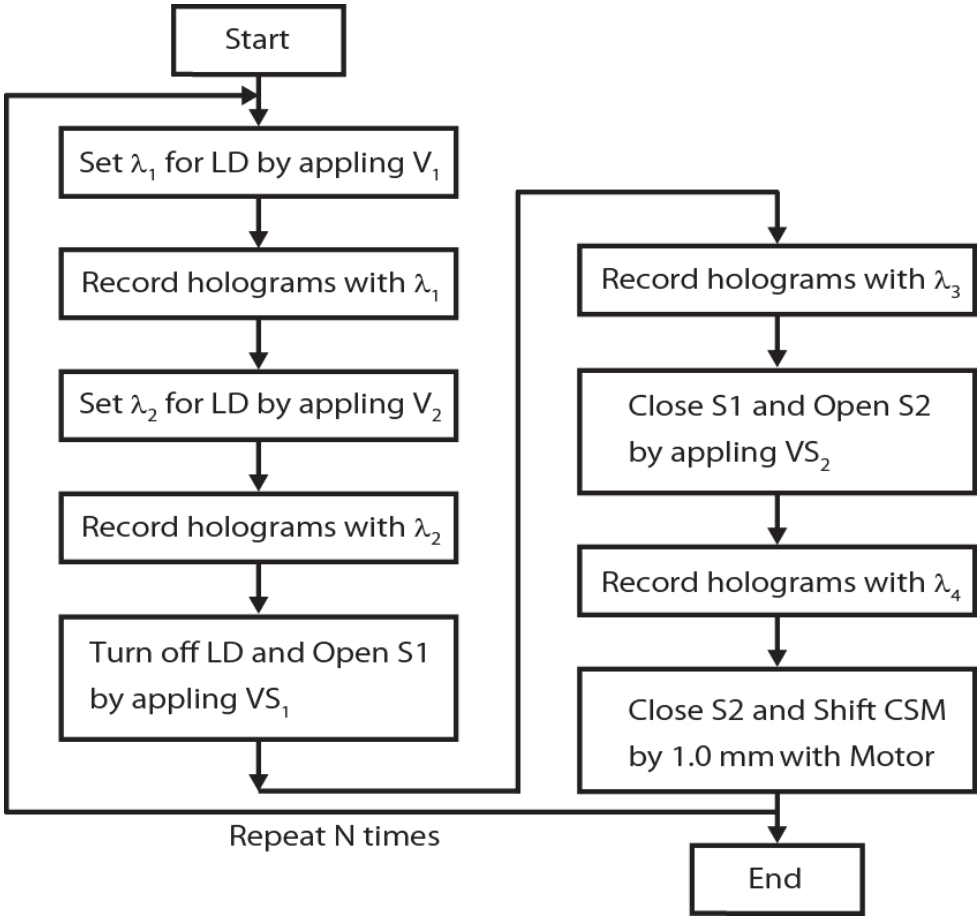

Fig. 3 Flow chart of the measurement process for a pipe inspection: $V_{1(2)}$, modulation voltage for the laser diode driver; $VS_{1(2)}$, control voltage for the electromagnetic shutter; S1(2), electromagnetic shutter.

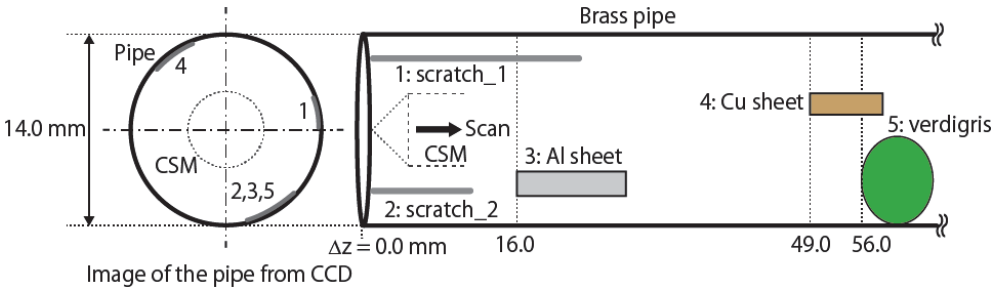

(a) Configuration of defects on the inner surface of the pipe

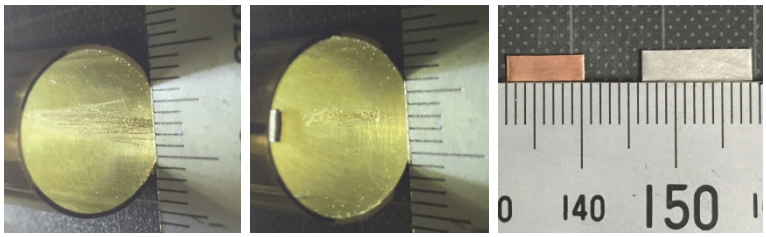

(1) Scratch_1 (2) Scratch_2 (3) Metal sheets

(b) Photograph of the defect on the inner surface of the pipe

Fig. 4 Defects of the brass pipe under test: (a) relative position of defects on the inner surface of pipe, 1, scratch_1; 2, scratch_2; 3, aluminum sheet; 4, copper sheet; 5, verdigris and (b) picture of the artificial defects: (1) scratch_1, (2) scratch_2, (3) metal sheets.

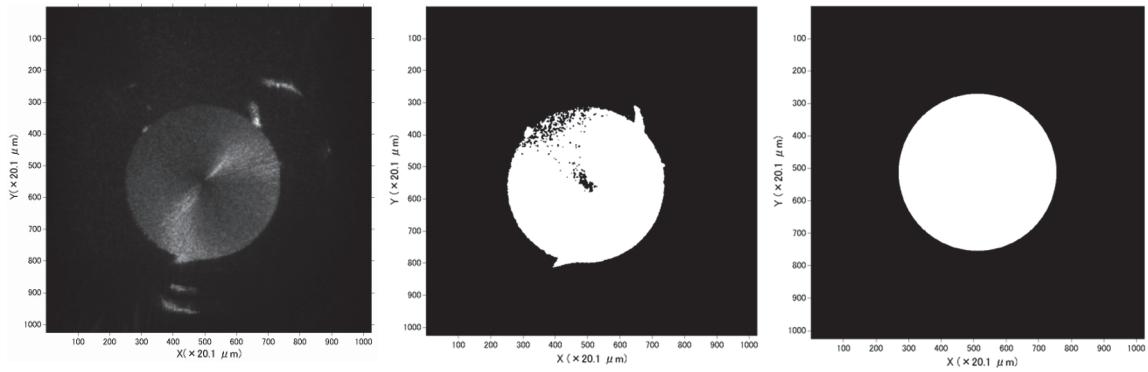

(a) Intensity image for λ_1 (b) Binarized image of (a) (c) Template image for (b)

Fig. 5 Example for evaluating the center of the reconstructed image using template matching technique: (a) reconstructed intensity image for λ_1 at Δz = 35.0 mm, (b) binarized image of (a), and (c) template image for (b).

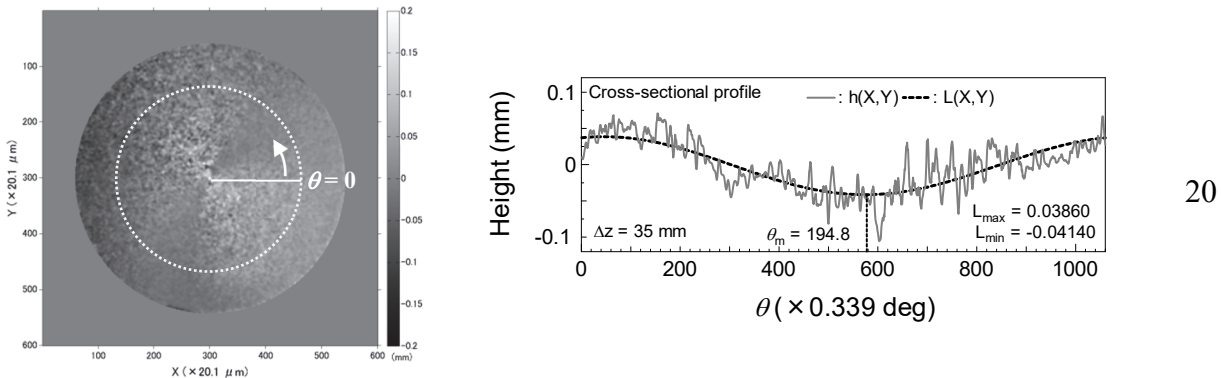

Fig. 6 Experimental height profiles obtained for the brass pipe at Δz = 35.0 mm: (a) the original experimental height profile $h(X,Y)$, (b) cross-sectional profile along the dotted line, (c) calculated optical path length $L(X,Y)$, (d) corrected height profile $h_c(X,Y) = h(X,Y)-L(X,Y)$, (e) cross-sectional profiles before and after correction.

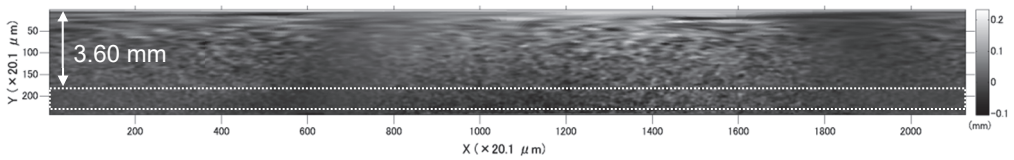

Fig. 7 Transformed rectangular image for Δz = 35.0 mm : the rectangular area having a width of 1.0 mm shown as dotted line was used for further analysis.

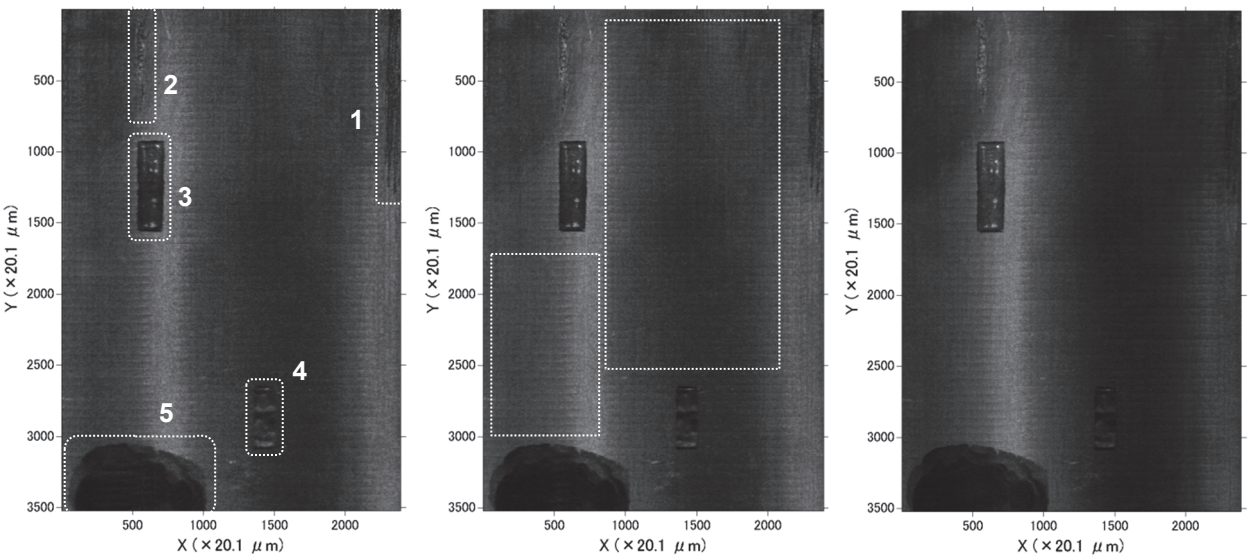

(a) λ_1 (b) λ_3 (c) λ_4

Fig. 8 Combined intensity images corresponding to the developed view of the inner surface of the brass pipe: (a) image for λ_1, (b) image for λ_3, and (c) image for λ_4.

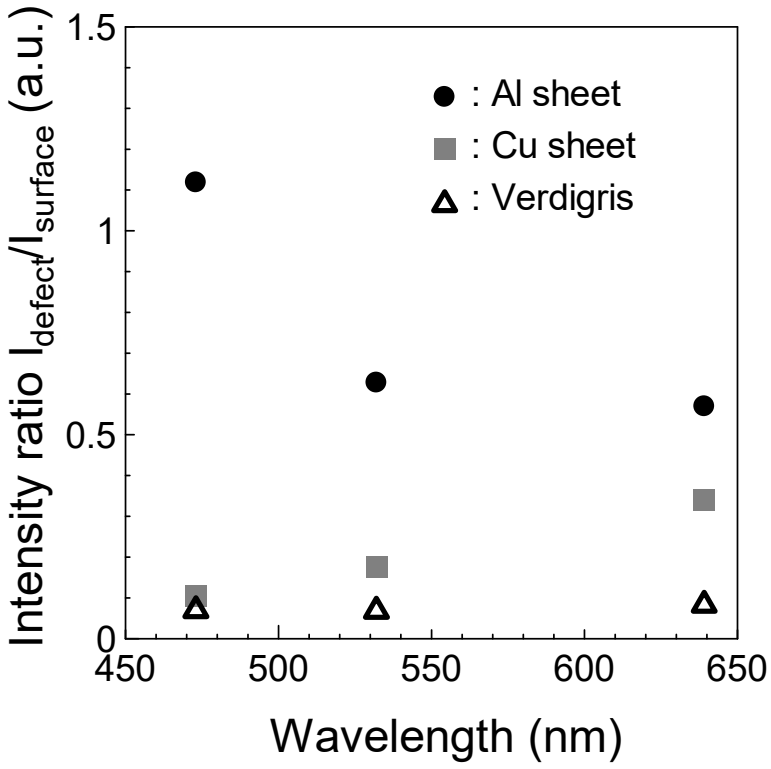

Fig. 9 Intensity ratio of $\overline{I_{defect}}/\overline{I_{surface}}$ calculated within the area of the artificial defects in the intensity images with wavelengths of λ_1, λ_3, and λ_4.

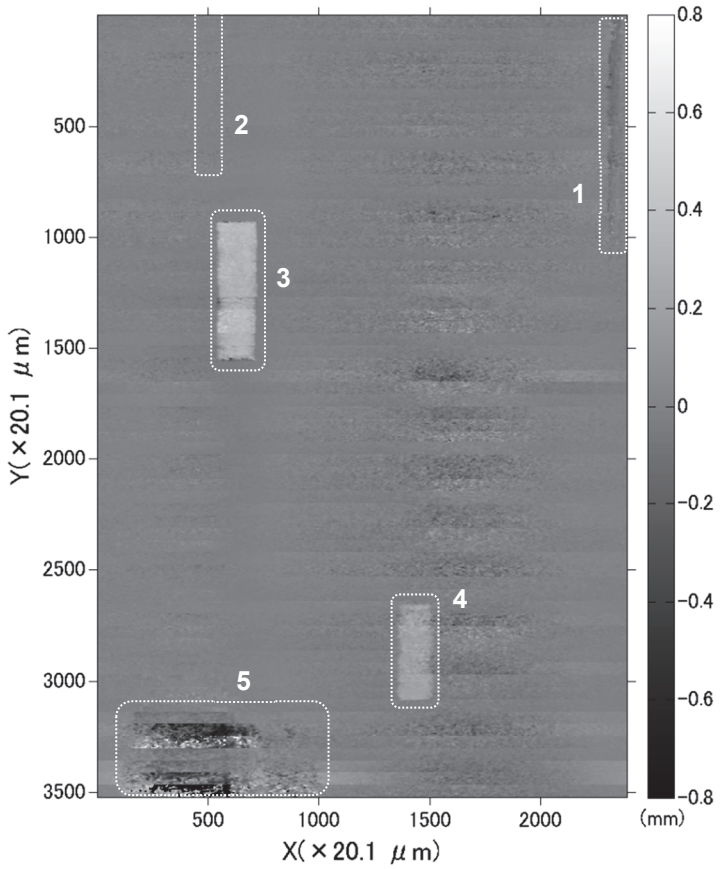

Fig. 10 Combined height profile image corresponding to the developed view of the inner surface of the brass pipe.

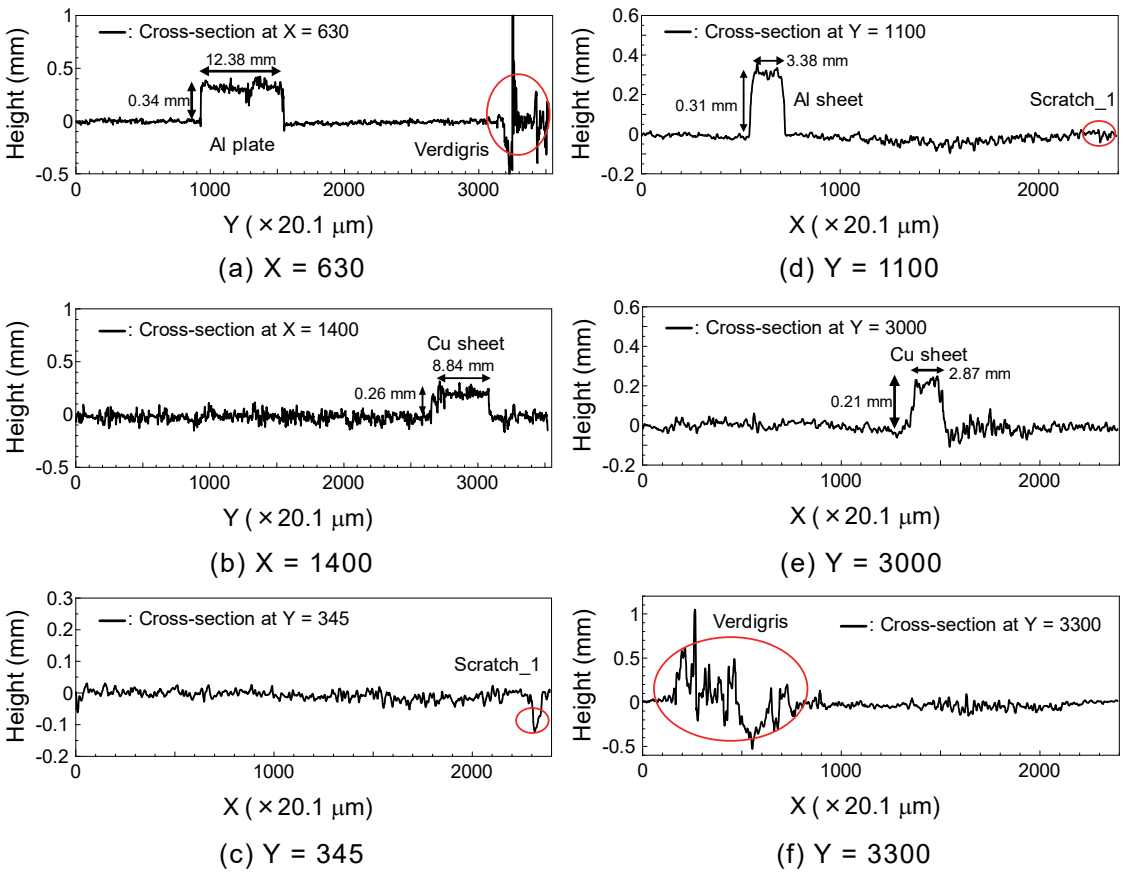

Fig. 11 Cross-sectional height profiles for the artificial defects in Fig. 9.

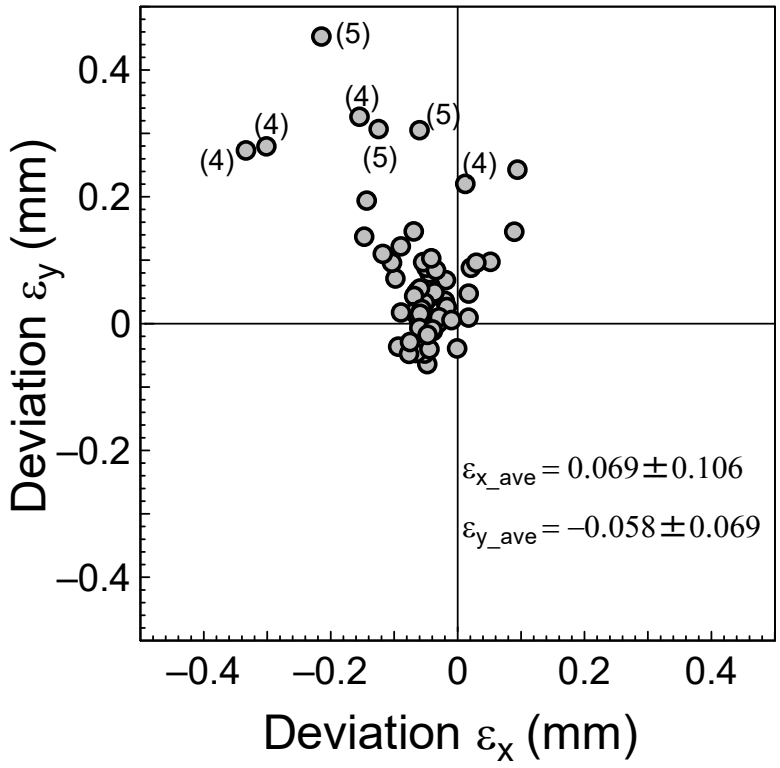

Fig. 12 Evaluated positional error of the CSM obtained by the new signal processing using the pattern matching method. The data having the number of 4 or 5 correspond to the areas including the defect of 4: Cu sheet or 5: verdigris.